An Eulerian-Lagrangian method for wet biomass carbonization in rotary kiln reactors

Salar Tavakkol [a,*], Thorsten Zirwes [a,b], Jordan A. Denev [b], Farshid Jamshidi [c], Niklas Weber [a], Henning Bockhorn [a], Dimosthenis Trimis [a]

[a] *Engler-Bunte-Institute, Karlsruhe Institute of Technology, Karlsruhe, Germany*
[b] *Steinbuch Centre for Computing, Karlsruhe Institute of Technology, Karlsruhe, Germany*
[c] *Institute of Digital Materials Science, University of Applied Sciences, Karlsruhe, Germany*

ARTICLE INFO

Keywords:
Biomass carbonization
Process optimization
Industrial-scale simulation
LES-MP-PIC
High-performance computing
OpenFOAM

ABSTRACT

This study presents numerical simulations of rotary kiln reactors for wet biomass carbonization. For this, a numerical tool has been developed resolving the carbonization process in time and space. Biomass particles are represented by Lagrangian particles that collide and form a moving bed. The gas phase is treated as an Eulerian phase. Both phases are fully coupled with the exchange of momentum, energy, and mass of chemical species. The tool is implemented in the open-source OpenFOAM® framework and additional submodels for devolatilization, drying and radiation have been developed for the conditions relevant during the carbonization process. In this way, models for the complex physical processes are combined in a single simulation tool.

A rotary kiln reactor of laboratory-scale is used to validate the numerical tool and to perform parameter studies to determine biomass conversion in dependence on the wall temperatures. The results also give insight into the sensitivity of biomass to carbon conversion with respect to the biomass moisture content and mass flow rate. The validated tool is used to perform simulations of an industrial-scale rotary kiln reactor, which are carried out on a supercomputer on up to 1120 CPU cores. The simulations demonstrate the effect of different wall temperatures on the optimal conversion of biomass to char and help to choose the optimal wall temperatures depending on the biomass properties.

1. Introduction

The utilization of lignocellulosic biomasses and biogenic wastes for energetic purposes and conversion to organic chemicals, syngas or charcoal has attracted increasing interest in the recent past. Particularly, thermochemical conversion of biomasses or biogenic wastes to charcoal increasing the energy density considerably and providing multi-purpose raw chemicals is being discussed intensively [1–4]. The thermochemical process focused in this study is steam-assisted carbonization, which upgrades low-energy density and wet organic feedstock in the absence of oxygen [5]. Carbonization is a kind of slow pyrolysis in which biomass is treated for 30–90 min at 250–400 °C in an inert atmosphere [6–9]. The superheated steam in the freeboard gas enhances the heat transfer and reaction kinetics [10]. To provide the superheated steam no additional gas input is introduced since the input biomass has high water content.

Compared to the virgin feedstock, the solid product has an increased carbon content as well as calorific value and its properties are similar to brown coal [11]. Unlike hydrothermal carbonization (HTC), the reaction time is relatively short, the process is continuous and operates at atmospheric pressure [6,12]. With this process, degradable wastes can be converted with high yield into stable bio-char of high energy density preventing their biological degradation [3,13,14]. Biomass degradation is a complex chemical process comprising multiple reaction pathways as well as products [2]. Therefore, biomass conversion mostly is described using simplified and formal reaction equations. The approach used in this work is given in section 2.3.4.

Current technologies for converting biomass to energy-densified products still face the complex nature of the various physical processes during wet-biomass carbonization, the characteristics of multiphase flow which is complicated to study experimentally [15], and the fluctuating parameters of the feedstock, e.g., moisture content, volatile fraction, size distribution, etc. [16–19]. These give rise to large uncertainties for designing and operating that process on an industrial

---

* Corresponding author.
E-mail addresses: Salar.Tavakkol@partner.kit.edu (S. Tavakkol), Thorsten.Zirwes@kit.edu (T. Zirwes), Jordan.Denev@kit.edu (J.A. Denev), Farshid.Jamshidi@hs-karlsruhe.de (F. Jamshidi), Niklas-N.Weber@t-online.de (N. Weber), Henning.Bockhorn@kit.edu (H. Bockhorn), Dimosthenis.Trimis@kit.edu (D. Trimis).

Abbreviations

CFD	Computational fluid dynamics
DEM	Distinct/discrete element method
DOM	Discrete ordinates model
DPM	Discrete particle model
FVM	Finite volume method
HTC	Hydrothermal carbonization
htc	heat transfer coefficient
MRT	Mean residence time
MP-PIC	Multiphase particle in cell
MS	Moisture content
PSD	Particle size distribution
RET	Radiative transport equation

Symbols

$\mathbf{a}_\mathrm{p}$	Particle acceleration
A_p	Particle's projected area
A_pc	Projected area of the cell
A_s	Particle's surface area
c_p	Heat capacity
C_∞	Vapor concentration in the bulk gas
c_i	Mass fraction of component i of biomass
D	Mass diffusivity
d_p	Particle's diameter
$\mathrm{d}t$	Timestep
E_a	Activation energy
$\mathbf{F}_\mathrm{c}$	Collision force
$\mathbf{F}_\mathrm{d}$	Drag force
$\mathbf{F}_\mathrm{g}$	Gravity and Buoyancy force
$\boldsymbol{g}$	Gravitational acceleration
h_fg	Enthalpy of water phase-change
h_s	Sensible enthalpy
h_tot	Total enthalpy
htc	Heat transfer coefficient
k_0	Frequency factor of Arrhenius approach
k_rxn	Reaction rate
k_C	Mass transfer coefficient
$\tilde{M}_{\mathrm{H_2O}}$	Molar weight of water
m_p	Particle's mass
$\dot{m}_\mathrm{dry}$	Drying mass rate
$\dot{m}_\mathrm{devol}$	Devolatalization mass rate
n	Order of the reaction
n_p	Number of particles in a computational cell
N_p	Molar flux of vapor
N_pp	Number of particles per parcel
Q	Transferred heat
$\dot{Q}$	Heat flux
Re_p	Reynolds number
$S_{\mathrm{p},h}$	interphase exchange source term for enthalpy
$S_{\mathrm{p},m}$	interphase exchange source term for mass
$\boldsymbol{S}_{\mathrm{p},mom}$	interphase exchange source term for momentum
S_rad	interphase exchange source term for radiation
S_{p,Y_i}	interphase exchange source term for species
p	Gas pressure
T_p	Particle temperature
T_g	Gas temperature
$\boldsymbol{u}_\mathrm{g}$	Gas velocity
$\mathbf{v}_\mathrm{p}$	Particle's velocity
$\boldsymbol{x}_\mathrm{p}$	Location of particle
Y_char	Mass fraction of char within a particle
$Y_\mathrm{vol.}$	Mass fraction of volatiles within a particle
$Y_\mathrm{moist.}$	Mass fraction of moisture within a particle

Greek letters

α_p	Volume fraction of solid particles
α	Diffusion coefficient for energy
ΔH_rxn	Enthalpy of reaction
ε_p	Particle's emissivity
η	Overall thermal efficiency
κ	Absorption coefficient of gas phase
κ^*	Modified absorption coefficient of gas phase
λ_g	Thermal conductivity of the gas
μ_g	Dynamic viscosity
ν_g	Kinematic viscosity
ρ	density
σ	Stefan-Boltzmann
τ	Stress tensor

Indices

k	Species
p	Particle
g	Gas
0	Initial state
final	Final state
mom	Momentum
conv	Convection
rad	Radiation
dry	Drying
devol	Devolatilization

scale.

The thermochemical conversion of biomass is governed by a large number of concurrent physical processes including the primary pyrolysis involving heating-up, drying, biomass particle shrinkage and chemical reactions. Radiative and convective heat transfer, as well as mass transfer under often turbulent conditions also have an impact. Experimental techniques developed in laboratory scales are difficult to scale up and are often based on empirical correlations. Scale-up can be supported by numerical simulations and models that reproduce the interplay of the aforementioned complex phenomena.

Numerical modeling and algorithms of multiphase flows have been developed continuously in recent years. For instance, a suitable approach to modeling two-phase dense flows is the Eulerian-Lagrangian method. Cundall and Strack [20] introduced an explicit Lagrangian numerical scheme for the distinct/discrete element method (DEM). The effect of fluid on the movement of granular particles in a horizontal pipe was included in the work of Tsuji et al. [21]. In this model, inter-particle forces were expressed by the Hertzian contact theory [22]. This method is limited to a low number of particles due to the computationally intensive neighbor-finding algorithm [21,22]. The DEM model is based on the soft-sphere model and allows precise simulation of the collisions [23]. But besides memory limitations for particle-based calculations, very small time steps are required to calculate the motion during collision [24].

To avoid these limitations, Andrews and O'Rourke [20,25,26] introduced the Multiphase Particle In Cell (MP-PIC) model where the particle motion includes particle-particle interaction. This interaction has been considered by incorporating the gradient of the solid stress as a force on the particle for dense particle flows with volume fractions above 5% [27,28]. Using the MP-PIC model, four-way coupling, i.e.

two-way interaction between the particulate and the continuum phase as well as particle-particle interactions in the moving bed, can be realized. Instead of resolving all particle collisions as in the DEM models, using solid stress makes the MP-PIC model considerably faster than DEM models for large scale simulations [29].

Earlier studies developed and verified models for biomass conversion in indirectly heated kilns using detailed chemistry coupled with conductive, convective and radiative heat transfer between bulk, gas and the kiln [30,31]. In those models, the biomass is modeled as a homogenous bulk in a one-dimensional plug flow reactor. However, to study the impact of size distribution, mixing and conversion of each particle, a more advanced approach is required that accounts for the individual treatment of the particles in the bed.

In this work, we present a solver that integrates models of all physical processes required for the simulation of three dimensional, time-resolved biomass conversion of moving particle beds in a single application. This is realized by combining OpenFOAM®‘s particle collision models (Discrete Particle Model, DPM and MP-PIC) for dense inert particle flows with OpenFOAM®‘s models for heat transport and chemical kinetics. Throughout this work, the MP-PIC collision model is used. Additionally in the appendix, a validation case with DPM is presented. The coupling in terms of momentum, energy and chemical species between the solid and the continuous gas phase is considered by four-way coupling. Submodels for heat transfer, moisture evaporation and devolatilization have been adapted and extended to conditions typically encountered during biomass conversion. All these submodels are validated against data obtained from own laboratory experiments.

After validation, the developed solver is used to simulate wet biomass carbonization in a laboratory-scale rotary kiln for a set of parameters with full biomass conversion. In a further step, the model is applied to a pre-defined industrial-scale reactor. Unlike the lab-scale simulations, polydispersed particles are considered. The main optimization parameter is the temperature of the industrial-scale reactor. The results are assessed in terms of the particle properties, e.g., size distribution and degree of conversion.

The average gas velocity originates from evaporation and devolatilization and corresponds to the laminar regime for the laboratory-scale. In the industrial scale kiln with a 15 times larger reactor diameter, slightly different flow regimes appear, and consequently, the flow in the industrial-scale reactor is in the transition regime and slightly turbulent. The turbulence model is additionally applied to ensure the consideration of localized turbulent flow induced by the particle bed as well as the consideration of higher rotational Reynolds numbers. Thus, the solver is adjusted to use fluid turbulence employing a Large-Eddy approach using the Smagorinsky sub-grid model. Because the simulation of the large-scale reactor requires the use of supercomputers, a study on numerical efficiency and scaling-up behavior is presented following the considerable advances and experiences on performance optimization in recent years reviewed e.g. by Ref. [29] as well as own experience in high-performance computing with OpenFOAM® [32,33].

2. Modeling & numerical simulation

2.1. Development of the solver

The main challenge of simulating biomass conversion in rotary kiln reactors is the complexity given by the large number of physical processes that need to be modeled. The open-source CFD framework OpenFOAM® [34] provides a large number of solvers for various engineering applications. However, to provide all capabilities required for the simulation of rotary kiln reactors additional models and components have to be complemented.

Two of OpenFOAM®'s standard solvers have been combined into a new solver (Fig. 1, left). The "coalChemistryFoam" module solves the Navier-Stokes equations and additional transport equations for energy and chemical species of the Eulerian gas phase. Additionally, particles are tracked in a Lagrangian reference frame and coupled with the gas phase. The Lagrangian particles are however only two-way coupled with the gas phase excluding particle-particle interactions. Therefore, the particle collision model from OpenFOAM®'s "MPPICFoam solver" has been implemented considering particle-particle collisions and therefore enabling the simulation of particle beds.

In addition, a new set of models has been developed (Fig. 1, right) and implemented. These include a new radiation model including the effect of dense particle flows instead of assuming infinitely small particles. A new single-step kinetic for carbonization of biomass based on an *n*-th order Arrhenius model is employed. An extension for non-spherical particles has been implemented as well. A new drying model is introduced extending OpenFOAM®'s drying model to full-steam atmospheres.

2.2. Governing equations

The gas-phase inside the reactor is modeled as the Eulerian phase and treated as an ideal gas mixture. The governing equations for total mass, momentum, energy and chemical species are:

$$\frac{\partial \rho_g}{\partial t} + \nabla \cdot \left(\rho_g u_g\right) = S_{p,m}, \tag{1}$$

$$\frac{\partial \left(\rho_g u_g\right)}{\partial t} + \nabla \cdot \left(\rho_g u_g u_g\right) = \quad \nabla p + \nabla . \tau_{eff} + \rho_g g + S_{p,mom}, \tag{2}$$

$$\frac{\partial}{\partial t}\left(\rho_g h_{tot}\right) + \nabla \cdot \left(u_g \rho_g h_{tot}\right) = \frac{\partial p}{\partial t} + \nabla \cdot \left(\alpha_{eff} \nabla h_s\right) + S_{p,h} + S_{rad}, \tag{3}$$

$$\frac{\partial \rho_g Y_i}{\partial t} + \nabla \cdot \left(\rho_g u_g Y_i\right) = \nabla \cdot \left(\rho_g\, D_{i,eff} \nabla Y_i\right) + S_{p,Y_i} \tag{4}$$

The subscript g indicates a quantity of the gas phase. ρ_g is the gas density, t the time, $\boldsymbol{u}_g$ the gas velocity and p the pressure. The subscript eff denotes the effective properties computed as the sum of molecular and turbulent transport properties. This affects the viscosity in the stress tensor τ_{eff} , the thermal diffusivity α_{eff} and species diffusion coefficient $D_{i,eff}$. $\boldsymbol{g}$ is the gravitational acceleration, h_{tot} the total enthalpy, h_s the

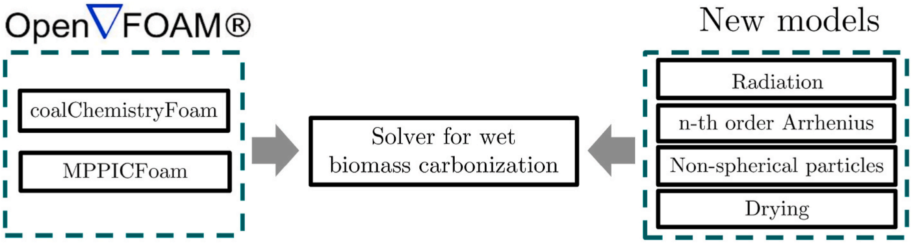

Fig. 1. Combining the capabilities of two existing OpenFOAM® solvers (left) into a new solver and development of physical models to correctly capture all processes in the reactor (right).

sensible enthalpy, S_{rad} the source term due to radiation and Y_i the mass fraction of the ith species. As gaseous species, N_2, O_2, CO_2, H_2O, CO and tar are considered.

The coupling between the Lagrangian particles representing the biomass particles is achieved by the source terms $S_{\mathrm{p},m}$, $S_{\mathrm{p},mom}$, $S_{\mathrm{p},h}$ and S_{p,Y_i}, which describe interphase exchange for mass, momentum, enthalpy, and species between gas and particles, respectively and are computed by the physical models described in section 2.3. The governing equations for the Eulerian phase are solved by the Finite Volume Method (FVM). Time is discretized implicitly using the Euler scheme and spatial derivatives are discretized by upwind and central schemes.

The Lagrangian particles are tracked in a Lagrangian frame of reference. The particle position $\boldsymbol{x}_{\mathrm{p}}$ is computed from

$$\frac{dx_p}{dt} = v_p,\ m_p\frac{dv_p}{dt} = F_c + F_g + F_d + F_p, \tag{5}$$

where m_{p} is the particle mass, $\mathbf{v}_{\mathrm{p}}$ the particle velocity, $\mathbf{F}_{\mathrm{c}}$ the collision force, $\mathbf{F}_{\mathrm{g}}$ the gravitational force. $\mathbf{F}_{\mathrm{d}}$ and $\mathbf{F}_{\mathrm{p}}$ are the drag force and the pressure gradient force, respectively, which have no considerable influence due to the operating parameters used in this work. Particles are assumed to be thermally thin, presupposing Biot numbers $Bi < 1$ for all particles. The Biot number is given by $Bi = \frac{htc\ d_p}{2\lambda}$, where $htc$is the heat transfer coefficient, d_p the characteristic length and λ the thermal conductivity of the solid. This definition of the Biot number follows Bryden et al. [35] which is used also by Ref. [36] because it accounts for a correction of the surface temperature due to the contribution of radiation. Estimating the $htc$to about 35 W/m^{2}K and the thermal conductivity of wet biomass to 0.25 W/mK, with the characteristic length of 0.9 cm the condition of $Bi < 1$ is fulfilled (the critical diameter of particles before drying is 1.4 cm and the largest particle in this study has a diameter of 0.9 cm (see Table 2)).

The improvement that could be gained through the temperature resolved model does not influence the end time of the reaction. This is due to the large pyrolysis number,$Py = \frac{\lambda}{k_{\mathrm{rxn}}\ \rho_p\ c_p\ d_p^2}$ determining the ratio of internal heat transfer and the rate of the carbonization reaction, which for the present work is approximately 10 (see Fig. 7). Therefore, in favor of computation efficiency, the thermally thin model is utilized while dealing with a large number of particles. The temperature of each particle is computed from

$$m_p c_{p_p}\frac{dT_p}{dt} = \dot{Q}_{conv} + \dot{Q}_{rad} \quad \dot{Q}_{dry} \quad \dot{Q}_{devol}, \tag{6}$$

where $c_{p_{\mathrm{p}}}$ is the heat capacity of the particle, T_{p} its temperature, $\dot{Q}_{\mathrm{conv}}$ the heat flux by transfer due to convection, where the convective heat transfer coefficients are computed from the Ranz-Marshall correlation [38]. $\dot{Q}_{\mathrm{rad}}$ the radiative heat flux is calculated through an enhanced variant of the discrete ordinate model accounting for the shielding of radiative heat transfer due to neighboring particles (section 2.3.5). In this model, contact heat transfer is assumed to be substituted by convection and radiation of neighboring particles within the same computational cell. Further clarification and support regarding this substitution are given in 3.3.2. $\dot{Q}_{\mathrm{dry}}$, the energy change during drying and $\dot{Q}_{\mathrm{devol}}$, the net energy change due to devolatilization are discussed in the next section. Drying and devolatilization are also the two processes by which the particle mass changes

$$\frac{dm_p}{dt} = \dot{m}_{dry} + \dot{m}_{devol} \tag{7}$$

The particle density ρ_{p} is assumed to be approximately constant, so that the particle diameter can be approximated from $d_{\mathrm{p}} = \left(\frac{6\ m_{\mathrm{p}}}{\pi\ \rho_{\mathrm{p}}}\right)^{1/3}$.

Due to the variation of thermophysical parameters for particles, e.g., thermal conductivity, the critical diameter of particles undergoing the reaction is different and smaller than that of the particles being dried. Considering the particle shrinkage, the largest particles in the solid phase are smaller than the critical diameter of 0.85 cm.

For the coupling of Eulerian and Lagrangian phases, the sources terms are described for the transfer of mass, momentum, heat and species in a specific computational cell i with the volume V_{cell} and applied to all N_p particles within this cell.

$$S_{p,m} = \frac{\sum_{i=1}^{N_p}\dot{m}_{dry,\ i} + \dot{m}_{devol,\ i}}{V_{cell}} \tag{8}$$

$$S_{p,mom} = \quad \sum_{i=1}^{N_p}\frac{F_d}{V_{cell}} \tag{9}$$

$$S_{p,h} = \quad \sum_{i=i}^{N_p}\frac{\dot{Q}_{conv} \quad \dot{Q}_{dry} \quad \dot{Q}_{devol}}{V_{cell}} \tag{10}$$

$$S_{p,Y_k} = \frac{\sum_{i=1}^{N_p}\dot{m}_{dry,i,Y_k} + \dot{m}_{devol,\ i,Y_k}}{V_{cell}},\ k = 1, 2, \ldots N_{species} \tag{11}$$

here $\dot{m}_{\mathrm{dry,i},Y_k}$ and $\dot{m}_{\mathrm{devol},i,Y_k}$ are the source terms of mass conversion for species k.

2.3. *Physical models*

The gas-phase transport properties (viscosity, heat conductivity, species diffusivity) are computed from the temperature-dependent Sutherland [37] model and enthalpy and heat capacities are computed from JANAF polynomials [38]. For the Lagrangian particles, drag force is computed from solid sphere drag, which plays a subordinate role due to the low gas velocities.

2.3.1. *Collision model*

The computation of collisions between solid particles consumes the main portion of the computing time due to a large number of particles. In OpenFOAM®, the discrete particle model DPM [39–41], where collisions are fully resolved, and the Multiphase Particle In Cell (MP-PIC) model, where collisions are approximated by a stress tensor, are implemented. In Ref. [42] the accuracy of both models has been evaluated against experimental data and the MP-PIC model has shown a much better computational performance with slightly better accuracy of average residence time compared to the DPM model. Therefore, the MP-PIC model is chosen in this work as a compromise between accuracy and computational effort. The limiting factor of both models is the size of the Lagrangian particles which cannot be larger than the cells in the computational mesh. The axial and transversal movement of particles within the bed is not prescribed by any bed-model, but the result of the collision model due to the resolved computation of forces for the solids movement.

2.3.2. *Non-spherical particles*

In OpenFOAM®, Lagrangian particles are assumed to be spherical, which is not true for realistic biomass feeds. The movement of the particles in the MP-PIC method is critical because it directly affects the resulting dispersion and mixing of the solid and the residence time of particles in the reactor. The simulated residence time of spherical wooden particles was in good agreement with experimental data [42]. The related results from Ref. [42] are summarized as supplementary material.

To adapt the MP-PIC model for non-spherical particles, an additional resistance force was introduced in Equation (5) that prohibits the quick rollout of particles from the inclined reactor. The approach represents the real biomass particles with unspecified geometries and comparable thickness to diameter ratio and helps to adjust the bed motion and the residence time of non-spherical biomass based on measured residence time. The enhanced friction method models the effect of non-sphericity and has proven to predict the correct particle behavior in experiments with prescribed residence time as well as the experimentally observed mixing without increasing the complexity of the simulation. The simulated residence time of real biomass particles with arbitrary geometrical parameters showed good agreement with measured residence times in the lab-scale rotary kiln at different inclination angles.

2.3.3. Drying model

The newly implemented drying model switches between a thermal drying model [43] and a Stefan-Maxwell based diffusion model [44] to allow a wide range of applicability. Additionally, the hygroscopicity of the biomass is taken into account by using the model of Stanish et al. [45] in Eq. (13). The modified thermal model assumes that drying occurs at the pressure-dependent boiling temperature $T_{\mathrm{boil.}}$ in a saturated atmosphere. $T_{\mathrm{boil.}}$ originates from the semi-empirical Antoine correlation [46]. The modified drying model additionally considers the evaporation below $T_{\mathrm{boil.}}$. The moisture evaporation rate is written as

$$\dot{m}_{dry} = \begin{cases} N_p \, A_p \, \tilde{M}_{H_2O} & , \quad T_p < T_{boil.} \\ \dfrac{\dot{Q}}{h_{fg} + \Delta h_{sorp}} & , \quad T_p \geq T_{boil.} \end{cases}, \tag{12}$$

$$\Delta h_{sorp} = 0.4 h_{fg} \left(1 - \frac{M_p}{M_{fsp}}\right)^2 \quad M_p < M_{fsp} \tag{13}$$

where A_{p} is the particle surface area; $\tilde{M}_{\mathrm{H_2O}}$ is the molar weight of evaporating species (water) and N_{p} denotes the molar flux of vapor, which is calculated for each particle from $N_{\mathrm{p}_i} = k_C(C_{\mathrm{p}_i} - C_\infty)$, where k_C is the mass transfer coefficient, C_{p_i} vapor concentration at the particle surface, calculated based on the saturated partial pressure of the evaporating medium at the surface temperature and C_∞ the vapor concentration in the bulk gas. $\dot{Q}$ represents the total heat delivered to the particle, the denominator of Eq. (12) reflects required enthalpy for the phase change and h_{fg} is the latent heat of evaporation. For moisture contents below the fiber saturation point, Eq. (13) adds additional heat of sorption δh_{sorp} to the enthalpy of phase change where M_{p} denotes the moisture content (dry basis) and M_{fsp} the moisture content at the fiber saturation point.

2.3.4. Devolatilization model

Studies of indirectly heated reactors like [30,31] presented and used comprehensive models for the decomposition of biomass which included high-temperature secondary tar cracking and competitive decomposition. Klose et al. [30] used these secondary reactions for tar and solid for operating temperatures of up to 800 °C. Babler et al. applied a two-step scheme of the pyrolysis model from Ref. [47] which is principally capable to simulate the decomposition with inert and reactive tar up to 700 °C. Morf et al. [48], however, stated that secondary tar reactions only become important when the operating temperatures exceed 650 °C. Due to lower operating temperatures, in this study, a simplified derivation of a previously developed model tailored to steam-assisted carbonization for the regarded condition is applied, in which secondary reactions are assumed to be negligible.

Based on experimental findings of Bockhorn et al. [9,11,49,50], a devolatilization model has been implemented based on a formal conversion equation

$$C_{6.0}H_{9.9}O_{4.4} \rightarrow 0.7C_{5.7}H_{7.85}O_{3.14} + 1.3H_2O + 0.2CO_2 + 0.3C_6H_6O_3 \tag{14}$$

and an *n*-th order Arrhenius approach:

$$\dot{m}_{devol} = k_0 e^{-\frac{E_a}{RT}} {m_v}^n {m_{v_0}}^{1-n}, \; \dot{Q}_{devol} = \dot{m}_{devol} \Delta H_{rxn} \tag{15}$$

Using this approach, the formed char is described by $C_{5.7}H_{7.85}O_{3.14}$ and the volatiles evolving during carbonization H_2O, CO_2, and tar are released to the gas phase and their share in the total amount of volatiles was determined by experiments resulting in Eq. (14). The component tar is represented as a virtual species with the properties of Hydroxymethylfurfural. In Eq. (15), $k_0 = 2.58 \times 10^{11} \frac{1}{s}$ is an effective pre-exponential factor averaged for the total amount of volatiles. Likewise, the activation energy $E_{\mathrm{a}} = 159.2 \times 10^6 \frac{J}{mol}$ and the reaction order $n = 1.22$ represent effective parameters. m_{v} is the volatile mass in the particle and $m_{\mathrm{v_0}}$ the total amount of volatiles. δH_{rxn} is the (endothermic) enthalpy of the over-all reaction determined to 194 $\mathrm{kJ/kg_{Feedstock}}$.

2.3.5. Radiation model

Heat transfer due to radiation is computed based on OpenFOAM®'s Discrete Ordinates Model (DOM) of the Radiative Transport Equation (RTE) [51,52] for discretized directions as well as local discretization. In the original implementation, solid particles are assumed to be small and their volume fraction is considered negligible in the cell. In the rotary kiln, however, the biomass particles form a multi-layer bed, where the different layers provide a shading effect. The absorption coefficient κ_{g}^* for a cell is computed from $\kappa_{\mathrm{g}}^* = \kappa_{\mathrm{g}}(1 - \alpha_{\mathrm{p}})$ in the original implementation, where κ_{g} is the absorption coefficient of the gas and α_{p} the volume fraction of solid particles in that cell. This is modified by using

$$\kappa_p^* = \frac{A_{pc}}{V} \frac{\min\left(A_{pc}, \sum A_{pp}\right)}{\max\left(A_{pc} - \sum A_{pp}, A_{small}\right)} \varepsilon_p \tag{16}$$

V is the cell volume, A_{pc} is the area of a cell projected to a discrete direction and $\sum A_{\mathrm{pp}}$ is the sum of all solid particle areas projected into that direction. The relative position of particles is considered by performing ray-tracing. While following a ray through the computational cells, the surface of particles within a cell is determined based on the sum of the projected area of all of the particles in that cell. This projected particle surface area is compared to the projected area of the cell in the direction of the ray to calculate the effective opacity of the cell and consequently the absorption coefficient of the solid phase. A_{small} is a numerical limiter to avoid division by zero. As the cell becomes filled with particles, the denominator approaches zero and κ_{p}^* becomes large, representing the effect of particles blocking radiation. The radiation between particles belonging to different cells is taken into consideration, however, all particles in the same cell are lumped together into an effective solid surface area. The absorbed radiation heat in a cell is distributed to the particles within that cell based on their average projected area. The emission is based on every particle's surface temperature and surface area. The emissivity of the particles ε_{p} is assumed to be unity.

3. Experimental setup and validation

3.1. Experimental setup

For the validation of the developed numerical tool, experiments in an indirectly heated laboratory-scale tubular rotary drum reactor by Carbolite Gero Ltd. (UK) have been performed. The length of the tube is approximately 1.4 m with an outer diameter of about 8.0 cm. The reactor provides a 1-m and 4.5 kW electrically heated zone, which covers the middle of the rotating tube (Fig. 2). Two sides of the reactor are cooled down by small blowers to prevent damage to sealings. The wet biomass enters the reactor through a hopper, as the only input. The gas-phase temperature is measured by thermocouples and solid products are collected at the outlet. The gas leaving the reactor is filtered and a Non-Dispersive Infrared Absorption (NDIR) analyzer BINOS® (Leybold-Heraeus, Germany) measures the CO and CO_2 concentration. For experiments with cold flows, the tubular reactor is exchanged by a glass tube which allows measurements of residence times and mixing behavior of the biomass by visual monitoring. The reactor rotates with a speed of 3–12 rpm and can be inclined between 0° and 5°. Typical biomass mass flow rates are between 1 and 15 kg/h.

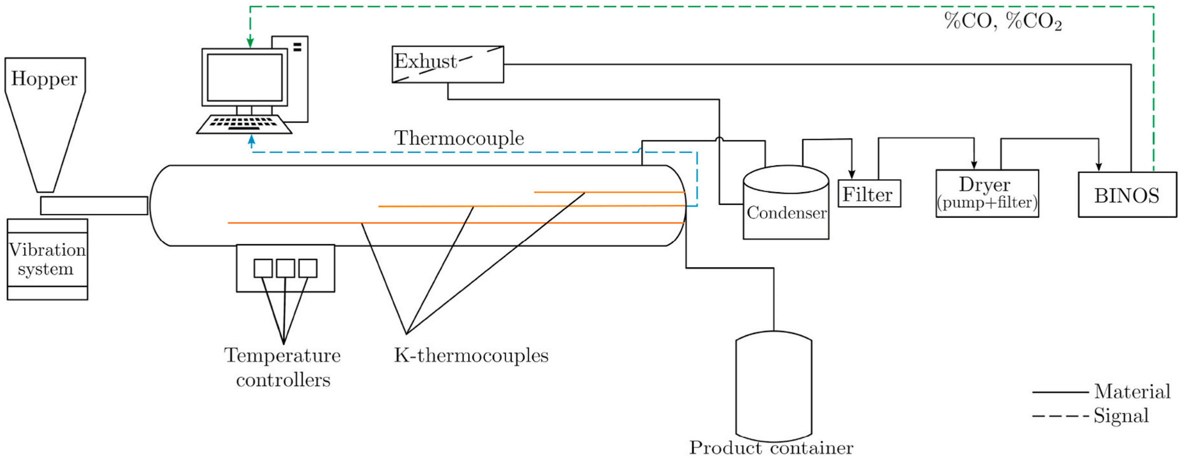

Fig. 2. Experimental setup for the lab-scale rotary kiln reactor.

3.2. Numerical setup

The computational domain is a cylinder of the same dimensions as the laboratory reactor and is made-up of 11,200 hexahedral finite volumes. The wall temperature is fixed to match the experiments. Fig. 3 shows the computational domain and an example of the wall temperature profile. At the inlet of the domain, biomass particles at a fixed mass flow rate are inserted. The reactor rotates with a prescribed velocity, which is implemented as a rotating boundary condition for the velocity.

3.3. Validation cases

3.3.1. Particle movement

The type of transversal movement within the particle bed effects dominantly the mixing and residence time of granular materials in rotary kilns and consequently, it determines the temperature gradient and the conversion of the solids in the bed [53]. To establish the type of movement of the particles in the rotary kiln for experimental work and the simulations, it is essential to define comparable criteria [54]. They can be in the form of critical wall friction coefficients and critical rotational Froude numbers in terms of the filling degree as given by the bed behavior diagram from Mellmann et al. [55,56].

For the lab-scale reactor, the Froude number is obtained to be about 1.2×10^{-4} representing a transition process between sliding and mixing motion. During the experiment with spherical particles and while using the glass tube, the sliding motion occurs which means the particle-wall friction is smaller than critical friction. On the other hand, the substitution of the metal tube in the heated kiln exhibits a slightly different motion as the spherical particles surge transversally. However, using real biomass particles with unspecified particle shape, the clear slumping/rolling types of motion is observed.

The movement of biomass particles in the rotating reactor can be simulated correctly [42]. Measured and simulated residence times of single particles and bulk movement are presented in the appendix for different reactor inclination angles and rotation speeds. The mixing due to particle movement inside the reactor has been measured with particles of different colors in Ref. [42] and the generalized mean mixing index [57] was determined. The simulations predicted the mixing index within 15% deviation compared to the experimental ones. In addition, the axial dispersion coefficients in the rotary drum were calculated based on the average velocity of particles. The values lie between $10^{-6} \frac{m^2}{s}$ and $10^{-5} \frac{m^2}{s}$ which is a common range of values in literature data [58].

3.3.2. Radiative and convective heat transfer

The radiative heat transfer model is tested for an artificial case of a bed consisting of 1800 particles with diameters of 1 cm in a box with 20 cm edge length. The temperature of the top wall of the box is set to 636 K and the other walls, as well as the particles, have a temperature of 373 K initially. As shown in Fig. 4, after 11 s the top layer of the particle bed has heated up, while the net heat flux between the bottom layer and the bottom wall is zero. Therefore, the effect of the particle bed on radiation is qualitatively captured.

In order to quantify the accuracy of the model, the heat flux from the top wall to the top particle layer is computed analytically from a view factor model [51]. The heat flow predicted by the newly implemented radiation model differs by approximately 1% in contrast to the original radiation model by OpenFOAM which yields a difference of about 15%.

The heat transfer coefficient (*htc*) due to convection is determined experimentally in the lab-scale rotary kiln reactor by inserting single wood particles with a moisture content of 50 wt.% and adjusting the residence time so that the particles leave the reactor with a remaining moisture content of about 25 wt.%. From the energy balance for the particles $Q_{convection} + Q_{radiation} - Q_{latent} - Q_{sensible} = 0$ the convective heat transfer coefficients are derived. Here $Q_{radiation} = \sigma \cdot \varepsilon \cdot A \cdot (T_g^4 - \overline{T}_p^4) \cdot t$ is used, where the particle emissivity ε is about 0.85 [59,60], the area of the particle is approximately constant and the mean temperature $\overline{T}_p$ is computed from the initial and final temperatures. Likewise, $Q_{sensible} = m_p \cdot \overline{c_p} \cdot (T_{p_0} - T_{p_{final}})$ is computed from the initial and final particle temperature and its mean heat capacity. Q_{latent} is determined

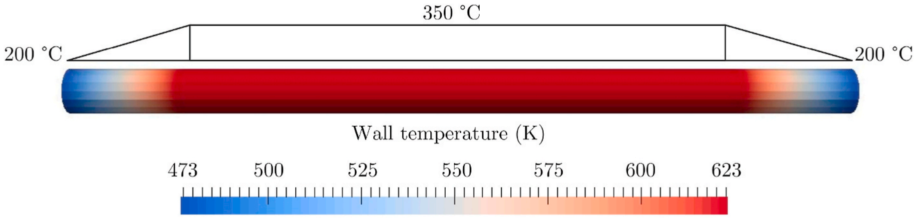

Fig. 3. Numerical setup of the full length 1.4-m lab-scale rotary kiln reactor. Linear temperature drop on both sides of the reactor based on the experimental conditions.

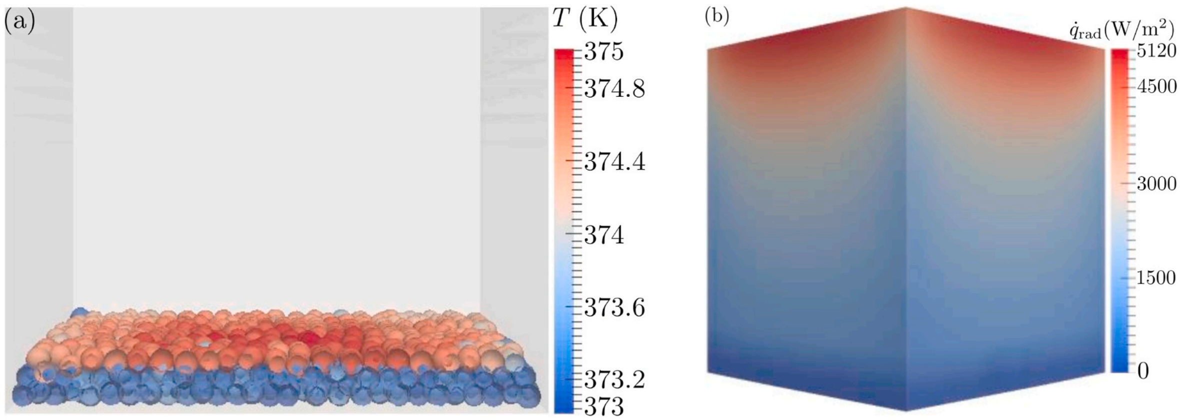

Fig. 4. Distribution of particle temperatures (a) and distribution of heat flux density on the side walls (b) during the box test with 1800 particles.

experimentally by measuring the evaporated water content from particles by multiplying the reduced weight of particles to the evaporation enthalpy. Fig. 5 shows measured and calculated *htc* values from an exact corresponding numerical simulation for different reactor temperatures using the Ranz-Marshall correlation. The Ranz-Marshall correlation calculates htc of each particle based on its Nusselt number, which is based on particles' Reynolds number. The figure demonstrates that the convective heat transfer model to the discrete phase for single-particle with low Reynolds number is reliable. Again, the simulated results lie well within the experimental uncertainties, which are obtained from 10 repeated measurements. This experiment and simulation are done for assessment of the precision and applicability of the Ranz-Marshall *htc* model for a single particle inside the reactor. Based on the observation of Wakao et al. [61], the Nusselt number for packed beds approaches the same limiting value from the Ranz-Marshall correlation for lower Reynolds numbers. In this study, the Reynolds number is generally low. Therefore, the Ranz-Marshall correlation is applied to both setups of single particles and particles in the bed.

McCarthy et al. studied the ratio of convective to contact heat transfer in rotary drums with similar parameters as applied in this study [62]. For conditions of low convective heat transfer coefficients and for particles with low thermal conductivity, e.g. biomass, the ratio of convective to conductive heat transfer is above 30 at 10 rpm. This holds even in the case of neglecting radiation in the rotary drum, whereas in the case of homogenous mixing the temperature distribution in the bed is more uniform. Therefore, the negligible influence of contact heat transfer in the well-mixed and high-temperature rotary drum can be assumed. Heat transfer between the walls and particles in contact with the wall is considered directly via radiation to the corresponding cell and indirectly via convection to the gas-phase and then to the discrete phase.

3.3.3. *Drying and devolatilization model*

The modified drying model has been validated in Ref. [42] demonstrating that the results match the analytical solution of a single particle drying in different atmospheres.

For validating the *n*-th order Arrhenius approach for the devolatilization, walnut shells (30 wt.% moisture content) at a mass flow rate of 0.58 kg/h are treated in the laboratory rotary reactor at residence times of 40–45 min and different reactor temperatures. The biomass is modeled as mono-sized particles with a diameter of 6 mm and the properties of the weight-averaged pseudo-component for the thermal degradation process (see section 2.3.4). The simulation has been performed for 1 h and the mass loss due to carbonization is recorded and compared with the measured mass loss, see Fig. 6. The results demonstrate that the *n*-th order Arrhenius approach from section 2 is able to predict the biomass conversion within experimental uncertainties for a large temperature range.

3.3.4. *Full process*

For validating the entire conversion process including heating, drying and devolatilization spherical wooden particles with a moisture

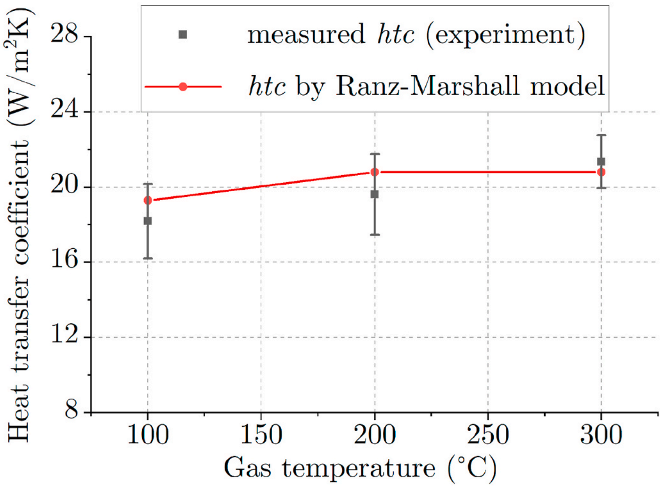

Fig. 5. Comparison of calculated and experimentally evaluated heat transfer coefficient for single spherical particles in a tubular reactor.

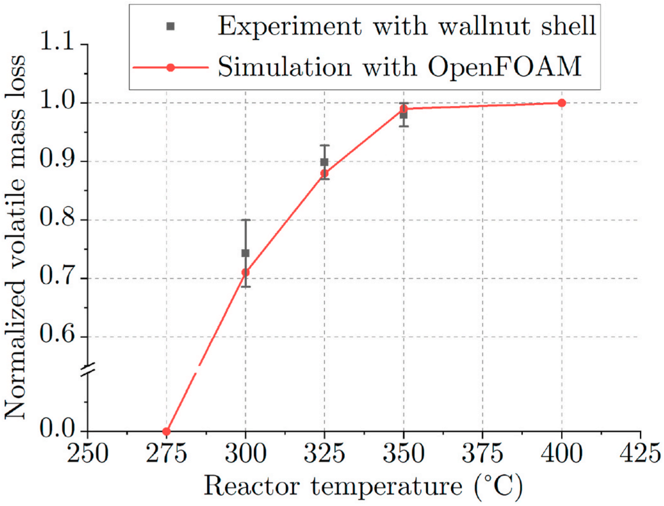

Fig. 6. Final normalized mass loss equivalent to the degree of conversion for different reaction temperature in experiment and simulation.

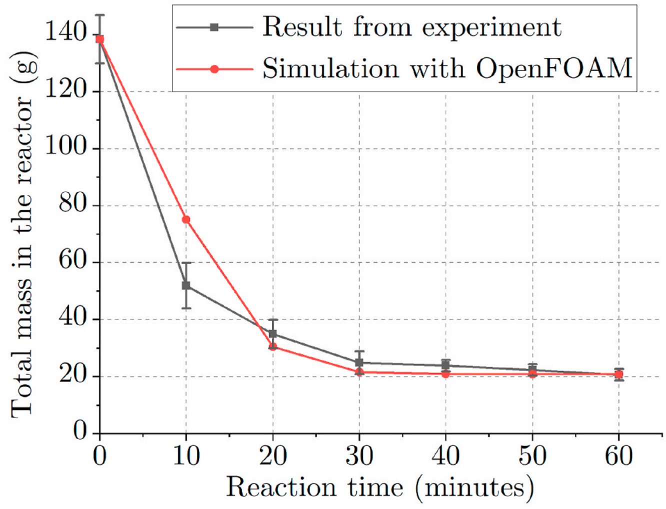

Fig. 7. Validation of the entire process with wooden spherical particles. Comparison of own experimental work with results from the developed solver based on OpenFOAM®.

content of 42 ± 4 wt.% are used as biomass feed. This feed is added batchwise. The operating conditions for the experiments are summarized in Table 1.

The effects of solids residence time at process temperatures of 350 °C are analyzed in Fig. 7. In these experiments, the total mass of the solid biomass is measured at different reaction times. The biomass input is heated up and moves along the reactor. The initial mass loss is due to drying. After five to 10 min, carbonization takes place and further reduces the mass. The comparison between experiment and simulation shows excellent agreement regarding the prediction of the reaction end time. The deviation at 10 min might be caused by simultaneous drying and carbonization, which is not sufficiently resolved by the applied drying and thermally thin particle models.

4. Results, discussion and scale-up calculations

The extended numerical tool is used for the simulation of the laboratory-scale rotary kiln and a large-scale rotary kiln. The two reactors are not the result of a correspondent scale-up. Both designs were determined by the plant builder before the study. The laboratory experimental setup is used to verify and validate the numerical simulation so that it can be used in the large-scale plant as well. The parameters for the simulations are given in Table 2. The results are presented in the following sections.

4.1. Laboratory-scale results

The laboratory kiln reactor rotates with a speed of 10 rpm and has an inclination angle of 0.5°–2.0°. This results in a mean residence time of 2700 s. Biomass as wooden bulk or other material with specified size ranges is fed into the empty reactor, which has a constant wall temperature. The simulations are performed until steady-state conditions. The results presented in the following refer to steady-state conditions. The definition concerning the full conversion of biomass in pyrolysis widely depends on material and research focus. In this work, the steam-assisted carbonization of biomasses is described by the conversion equation Eq. (14). and the corresponding kinetics Eq. (15). With this, the conversion in dependence on mean reaction time can be calculated.

Table 1
Summary of operating conditions for the validation test.

Biomass input		Reactor	
Input mass (g)	138 ± 8	Wall temperature (°C)	350 °C
Initial temperature (°C)	25	Pressure	atmospheric
Moisture content wt.%	42 ± 4	Length (m)	1.4
Dry mass (g)	80.0 ± 0.2	Diameter (cm)	8.0 cm
Volatile fraction (wt.%)	75	Rotation (rpm)	10 rpm
Particle diameter (mm)	6.0	Inclination (°)	3
Heat of reaction (kJ/kg)	400	Gas input	none
particle density (kg/m^3)	1224.7	Gas output	to condenser
Dry mass c_p (J/kg.K)	2000	Coal-collector	purged with N_2

Table 2
Parameter study of lab-scale and large-scale rotary kiln reactor for wet biomass carbonization.

Size	Wall Temp. (K)	Mass flow rate (kg/h)	Moisture content (%)	Particle size (mm)
Lab-scale	573	0.580	50	6
	598	**0.580**	**50**	**6**
		1.160	**0, 10, 20, 30, 50**	
		1.760	**50**	
	623 673	0.580 0.580	50 50	6 6
Large-scale	673 723 773 873	350	50	Normal distribution expected: 6, variance: 2, range: 1-9

4.1.1. Influence of the reactor wall temperature

The different stages of the carbonization process undergone by the discrete phase are shown in Fig. 8 at steady-state conditions (physical time 3600 s). The left indicators represent the length of the reactor (*z*-direction) and the Mean Residence Time (MRT≈2700 s) of the particles. Different zones in this work are determined from post-processing, and they are not a part of the numerical model assumptions or a priori domain division. In the heating up zone (blue region), the mass of

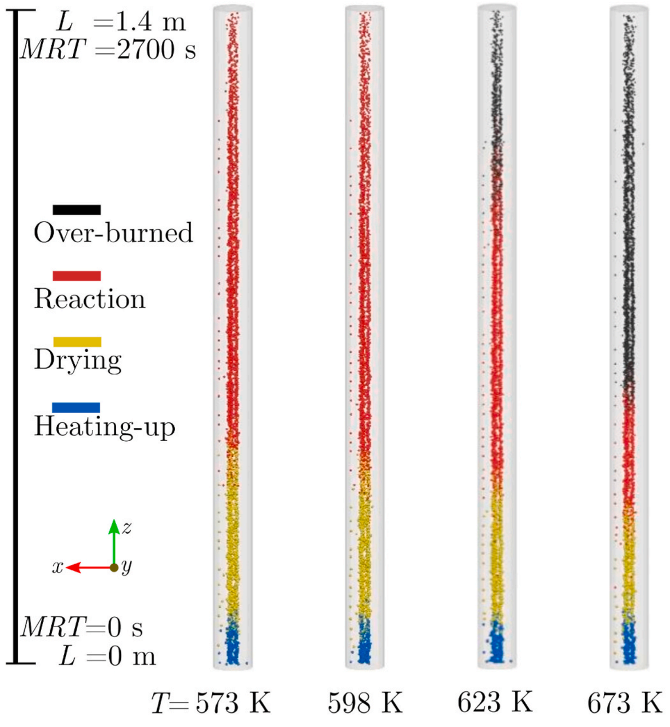

Fig. 8. Four stages of the process in the rotary kiln at different wall temperatures (top view).

particles does not change while their temperature increases. In the drying zone (yellow region), the moisture content (MS) of particles is decreased to zero by evaporation/vaporization. After drying, devolatilization starts (red region), where particles release volatiles (tar, H_2O and CO_2) and lose further mass. Reaching the final mass of the particles, the over-burned stage (black region) shows a further increase in temperature. Other possible changes in product properties along the over-burned zone are not in the focus of this study and therefore are omitted, although, in reality, further secondary reactions may occur. The goal of the process is to achieve a full conversion and to minimize biomass in the over-burned state.

The heating-up zone is relatively short compared to other zones. The carbonization is kinetically limited and therefore the reaction zone is comparatively long. At a wall temperature of 573 K, a final conversion of 71% is attained and reaches 88% and 99% at wall temperatures of 598 K and 623 K, respectively. On the other hand, at the highest temperature, not even half of the reactor length is required to complete the conversion.

The optimum wall temperature for the lab-scale reactor is 623 K, where the reaction is completed at the end of the kiln and only a short over-burned zone exists. The conversion is very sensitive to the wall temperature. The final conversion of the particles is also given for each case at the right-hand side of each case in Fig. 9.

4.1.2. *Influence of mass flow rate*

In Fig. 10, the influence of the biomass mass flow rate is illustrated for the reactor with the wall temperature of 598 K and the initial moisture content of particles of 50%, see also Table 2. The final conversion strongly depends on the length of the contact between the bulk and the hottest freeboard gas. Due to the high energy consumption of the process, a larger mass flow rate increases sharply the required heat and consequently limits overall conversion. The analysis of the influence of the mass flow clearly shows that the reactor is under heat transfer limitation by higher mass flows. This is due to the heat transfer limitation within the reactor since the constant wall temperature is maintained.

Initially, the gas phase in the reactor consists of dry air. During the drying phase, the air is gradually displaced by moisture and later partly by volatiles. Under steady-state conditions, only water vapor and volatiles are present in the gas phase and the mass fraction of non-condensable volatiles is $1 \quad Y_{\mathrm{H_2O}}$. With the lowest particle mass flow rate in Fig. 11 (top), the carbonization reaction starts within the first half of the reactor and the mass fraction of volatiles grows suddenly near the bulk and is diluted gradually in the moisture from the drying zone. By raising the mass flow rate, the moisture released from the bulk displaces a larger volume in the reactor. Due to the same wall temperature in all cases, the volatile release is postponed and the reaction zone is shifted towards the end of the reactor. With mass flow rates above 2 kg/h, devolatilization does not start as far as the biomass is in the reactor.

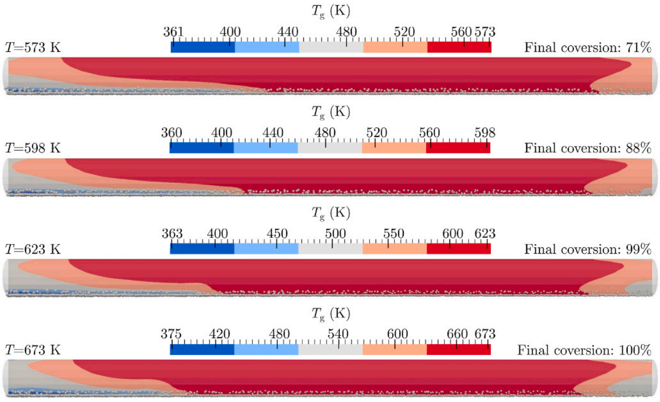

Fig. 9. Gas temperature on a cutting plane through the center of the rotary kiln for different wall temperatures (side view). Here and in all consequent figures, the bulk and gas move from left to right.

4.1.3. *Influence of moisture content*

Fig. 12 depicts the influence of the initial moisture content (MS) of biomass particles on the gas temperature at a constant reactor wall temperature of 598 K and a mass flow rate of 1.160 kg/h. Raising the MS at a constant mass flow rate shows a similar effect on the gas temperature as raising the mass flow rate at the constant moisture content (compare with Fig. 11). However, while raising the MS, the final conversion is first slightly increased although one may think about the downtrend.

This effect on final conversion is due to an increased heat transfer coefficient in the presence of higher MS in the freeboard gas. In this case, the larger c_{p_g} of steam leads to a higher Prandtl number. Consequently, the Nusselt number increases resulting in a higher heat transfer coefficient of particles. Additionally, the larger heat capacity of the gas keeps the temperature higher during the heating of cold/wet biomass bulk which leads to an increase in the overall heat transfer to the bulk.

The overall conversion rate of cases with MS 0% and 10% from Fig. 13 proves that despite the increase in total required heat, the gain in the interphase heat transfer dominates. The difference between the final conversion of the cases with MS 0% and 30% is unexpectedly small, see Fig. 13. The reason for this is that a large zone of the reactor (heating up and drying zone) is completely filled with the super-heated steam $Y_{\mathrm{H_2O}} = 1.0$.

4.2. *Scale-up motivation & process optimization*

The simulations of the large-scale reactor require considerably larger computational resources. In order to find an optimal setup, a grid independence study is carried out. The finest computational mesh consists of 2,700,000 hexahedral control volumes with an average edge size of 2 cm. The total length of the reactor is 12 m. This is the finest possible mesh resolution due to the restriction from particle volume fractions in a cell (section 2). A coarser mesh with an average edge size of 4 × 4 × 4 cm is composed of 375,000 cells. Comparing with the finest mesh, the relative deviation in time-averaged gas temperatures at the centerline of the reactor is only about 0.30% after 230 s physical time. Therefore, the latter grid which accelerates the simulation 8.45 times is chosen for the large-scale simulation as a compromise between precision and performance. Other mesh resolutions with average edge sizes of 2 × 2 × 5 and 2 × 2 × 10 cm have also been studied but their precisions, despite the higher resolutions, is lower than that of the 4 × 4 × 4 cm cell grid. This emphasizes that the aspect ratio of cells is a decisive factor. The numerical grid is adopted to resolve the eddies with the largest scale within this particular application and except mesh resolution study, the longitudinal integral length scale criterion from Kim et al. [63] is considered.

The CPU performance for the computation of the disperse phase using the MP-PIC method is tested for a short simulation with 2 s physical time and increasing the number of particles from 5000 to 450,000 in 11 steps. The computation effort increases linearly with the number of particles in the domain. For a single CPU, the average execution time per timestep grows from 5.1 s to 31.2 s for the smallest and largest number of particles, respectively. In contrast to the lab-scale simulations, where each parcel represents one particle, in the large scale simulations, parcels with 10 particles are modeled for a feasible computational performance. In the steady-state condition, there are more than 3,330,000 particles in the domain at the same time. On the other hand, it was found in Refs. [42] that the computation time of the DEM-based model in the lab-scale grows exponentially with the number of particles. Even applying the reduced particle stiffness model suggested by Ref. [64] to the DEM, it is still computationally expensive for large-scale simulations.

In the modified fvDOM radiation model, 72 global spatial directions for ray-tracing are used to calculate the radiation field in each 20th

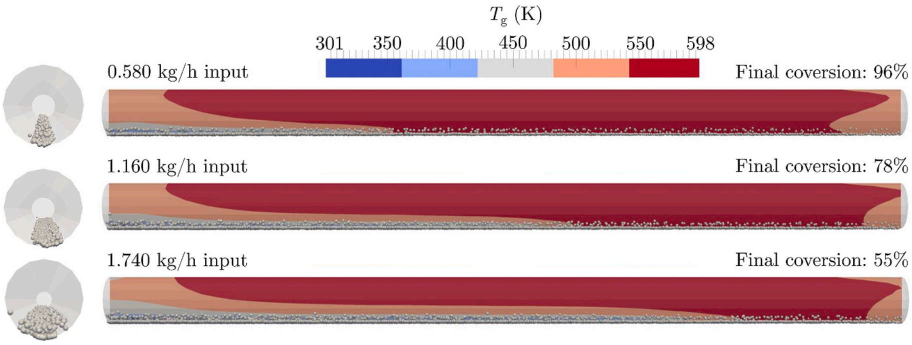

Fig. 10. Gas temperature on a cutting plane through the center of the rotary kiln at different mass flow rates (side view).

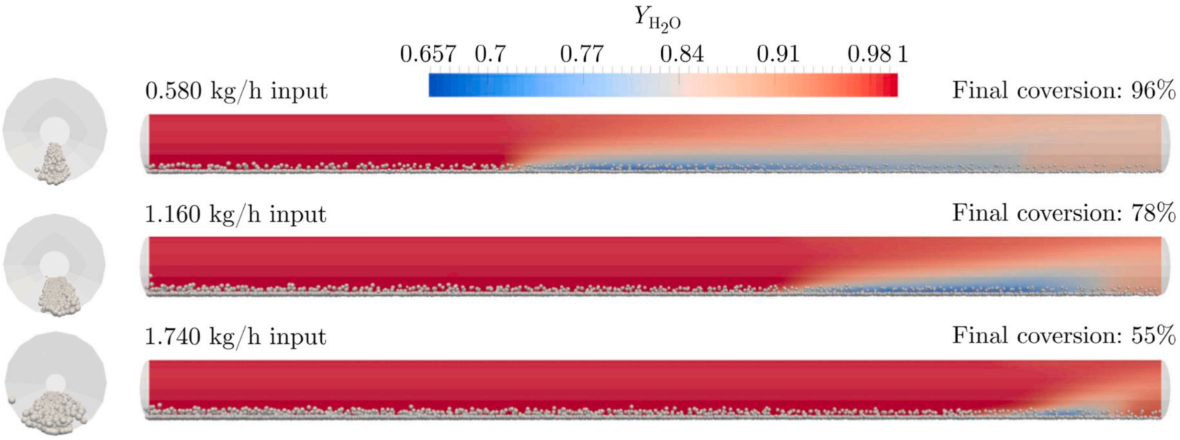

Fig. 11. Moisture mass fraction Y_{H_2O} on a cutting plane through the center of the rotary kiln at different mass flow rates (side view).

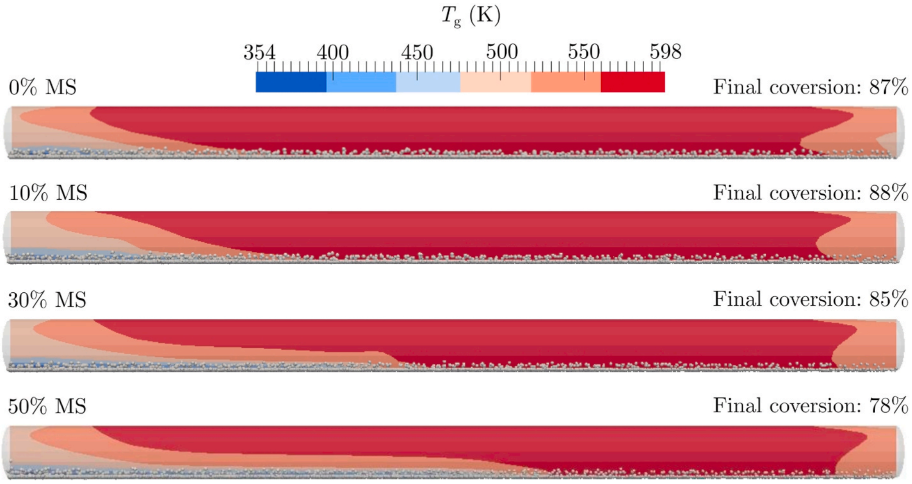

Fig. 12. Gas temperature on a cutting plane through the center of the rotary kiln at the different MS (side view).

timestep (solver frequency of 20). The results are compared to the refined case with 128 directions and the solver frequency of 1. Only 2.5% decrease in average particle temperatures is observed while the computation time is reduced by a factor of 7.

For the large-scale simulations, the performance of the parallel runs is tested with 2 up to 1120 CPU cores on the high-performance computer "bwUniCluster 1.0". Reasonable parallel scaling is observed up to 560 cores. The total amount of CPU-hours for each simulated case with different temperatures is around 40,000.

The operation parameters for the large-scale rotary kiln are taken according to those of the laboratory scale rotary kiln. The residence time of the bulk is taken from the lab-scale simulation based on the experimental study of the kinetically limited carbonization reaction to ensure the reaction is completed [9,49,50]. Although most parameters such as particle composition, MS, initial temperature, reaction mechanism, etc. are taken from the former, the filling degrees between the lab-scale (14%) and large-scale (4.4%) are different. This is because the biomass particles in the lab-scale and the large-scale reactor have the same MRT, but the mass flow rate is higher by a factor of 350 in the large-scale reactor (Table 1). Considering a comparable heat transfer

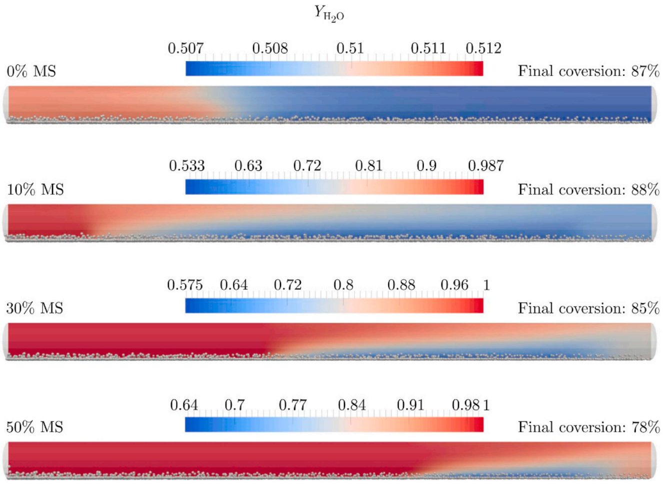

Fig. 13. Gas MS on a cutting plane through the center of the rotary kiln at different initial MS of particles (side view).

coefficient for kilns, the main concern is the final product quality. To satisfy the energy-intense process, a larger area for the heat transfer and therefore a comparably larger kiln is required.

The gas velocities within the reactors are generally low. For the laboratory-scale case, the average gas velocity is around 0.1 $\frac{m}{s}$, while it is in the order of 0.12$\frac{m}{s}$ in the industrial scale kiln. This corresponds to Reynolds numbers $Re < 200$ for the laboratory-scale and $Re \approx 3050$for the large scale with 15 times larger diameter. An additional simulation without turbulence model has shown that the difference in heat transfer coefficients is below 5%. This shows that the turbulence model does not change the results qualitatively and both scales are still comparable.

4.3. Large-scale results

The large-scale reactor has a length of 12 m and a diameter of 1.2 m and rotates with a speed of 10 rpm. For the large scale, the rotation of below between 3 and 5 rpm is common for rotary kilns with built-in installations [53,54]. Since the large-scale reactor does not have a shovel or internal flights in the simulation but instead is a cylinder, the larger rotational speed is applied for comparable mixing in the numerical setup. However, based on the bed behavior diagram from Henein et al. [49] the bed motion is still in the same regime regardless of 10 or 3 rpm, where the Froude number lies in the range of $10^{5} < Fr < 10^{3}$ associating an analogous bed motion to the lab-scale reactor with metal tube and therefore this overdesign has negligible implications. A polydisperse distribution for biomass particles is considered in the kiln (see Table 2 and Fig. 17).

The wall temperature of the kiln is chosen for the parameter study. A uniform wall temperature is considered for the entire wall of the reactor. The results presented in the following are for different wall temperatures from Table 2 at steady-state conditions. Also, transient results for a specified case with the wall temperature of 773 K are illustrated in order to show how the steady-state is reached.

4.3.1. Transient study of gas-phase parameters

4.3.1.1. Gas-phase temperature. Fig. 14 presents the time evolution of the gas temperatures at a central rectangular cutting plane of the tubular kiln reactor as well as at 7 cross-sectional planes at a distance of 2 m each. A homogenous temperature profile can be seen in locations far from the bulk. However, after the drying zone, the gas temperature near particles shows a uniform profile. The radial homogeneity of the temperature field in the reactor is enhanced compared to the lab-scale device. After 1800 s the temperature profile approaches the steady-state and there are no significant variations in the gas temperature distribution except at the low-temperature region (blue range, due to wet particles) which expands towards the exit. The gas temperature near the outlet is close to the corresponding wall temperature at all times.

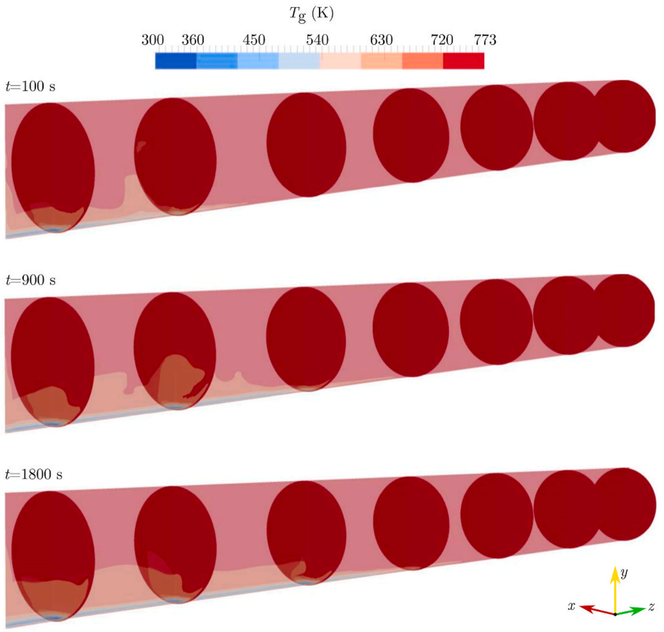

Fig. 14. Gas temperatures at an axial cutting plane through the center and cross-sectional planes in the large-scale rotary kiln at different times (isometric view).

Although the freeboard gas is initially at room temperature, the simulation with constant wall temperature results in rapid heating of the gas (100 s). At the beginning, the O_2 and N_2 contents in the freeboard gas are 0.21 and 0.79, respectively. During the process, moisture and volatiles substitute the initial gas while the atmospheric pressure pushes the gas out of the reactor through the outlet patch. After approximately 1800 s, there is no air/oxidizing agent in the reactor anymore.

4.3.1.2. Volatiles mass fraction. The time evolution of the tar mass fraction Y_{TAR} of the gas phase is illustrated for the case study with the wall temperature of 773 K in Fig. 15. At 400 s, the devolatilization is observed between 6 and 8 m (3rd and 4th planes). However, at later times, the devolatilization starts further downstream while a higher volume is filled with volatiles. The tar mass fraction reaches the stationary state after around 1800 s in this case as well. The distribution of CO_2 is the same as tar and only its magnitude differs due to the lumping of the volatiles.

4.3.1.3. Accumulated mass of by-products. Fig. 16 shows the moisture release (a) and volatile release (b) from the solid phase at different temperatures. The rate of moisture released from the bulk shows an expected increase when increasing the wall temperature of the reactor. At 773 K a small decrease is visible in the drying rate at around 3000 s as the bulk mass increases in the reactor constantly. The trend in the first half of the simulation is closer to that of 873 K. By increasing the mass input, however, the colder gas moves more rapidly in the reactor and consequently, the heat transfer limitation in the drying zone slows down the drying rate.

Fig. 16b shows the development of volatile release. The cases 673 K, 723 K and 773 K reach their stationary states while the rate of 873 K is still on a slight non-linear rise. The accumulated volatile release in the reactor at 673 K after around 1500 s remains constant because the unsatisfactory heat transfer is not initiating chemical conversion of the biomass. At this temperature, the total amount of supplied heat is used

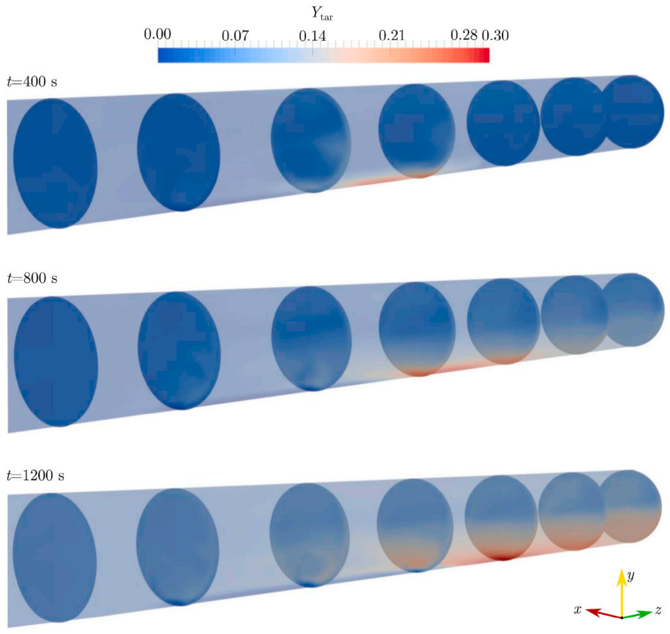

Fig. 15. Tar mass fraction at an axial cutting plane through the center and cross-sectional slices with the wall temperature of 773 K (isometric view).

for heating-up and drying.

4.3.2. Steady-state results for large-scale simulations

4.3.2.1. Influence of the wall temperature on carbonization. For the large-scale simulations, particles are used, which initially contain the mass fraction of moisture $Y_{\text{moist}} = 0.50$, volatiles $Y_{\text{vol.}} = 0.25$ and fixed carbon and ash $Y_{\text{char}} = 0.25$. Ideally, the char mass fraction of particles leaving the reactor is $Y_{\text{char}} = 1.0$, which can be observed for the cases where the wall temperature lies above 723 K, see Fig. 17a giving the results for stationary conditions (3600 s).

In contrast, the conversion degree for the wall temperature of 673 K is not satisfying, as the graph shows more than 50% of particles leaving the reactor are not even completely dried since their Y_{char} is below 0.5. Increasing the reactor temperature to 723 K, the conversion to charcoal is improved. Around 92% of particles already reach the desired mass fraction $Y_{\text{char}} \geq 0.90$.

Fig. 17 suggests that the wall temperature in the ideal case should be between 723 K and 773 K. Therefore, these two cases are further referred to “the optimal wall temperature cases”. Seasonal or material-related variable parameters such as MS and input temperature of the biomass would require further adjustments of the wall temperature.

4.3.2.2. Influence of particle size on the product at different wall temperatures. The variation of the particle sizes calculated with the constant density model (see section 3.2) are depicted in Fig. 17b for stationary conditions. The size distribution is shifted to smaller sizes when increasing the wall temperatures due to increasing release of moisture and volatiles.

The effect of particle sizes on their temperature distributions along the reactor is shown in Fig. 18. The PSD is divided into the small fraction (smaller than 5 mm) and the large fraction (larger than 5 mm). The particle size has no influence on the conversion of the bulk in different lengths of the reactor. This means, that due to the good mixing in the bulk, the particles with different sizes have an identical temperature in each longitudinal section of the reactor. Similar behavior is also observed during the conversion of biomass in the experimental work on the lab-scale reactor where the carbon content of the char exhibits good product homogeneity and a standard deviation being less than 2.7%.

4.3.2.3. Analysis of the process stages along the reactor. For the investigated temperatures, similar to the lab-scale, four zones/stages are introduced (compare with Fig. 8). To compare the two scales, it is worth mentioning that the range of wall temperatures in the large-scale simulations in Fig. 19 (673–873 K) is considerably higher than the range in the lab-scale simulations in Fig. 8 (573–673 K). At the same wall temperature (673 K) and the same MRT (2700 s), the laboratory and large-scale reactors show different behaviors: while the biomass in the lab-scale reactor reaches the over-burned state at the end of the reactor, the reaction has not even started in the large-scale reactor even with a significantly smaller degree of filling. This demonstrates, that the scaling-up behavior cannot be predicted directly from the laboratory-scale results and full simulations of the large-scale reactor are necessary.

At a wall temperature of 873 K, only 7 m of the reactor are used to complete the biomass conversion as defined in this study. Further reactions related to this temperature, e.g., secondary cracking and other exothermic decompositions are neglected, as explained previously in section 4.1. This impacts negatively the desired state of the product and additionally increases energy consumption. The optimum wall temperature lies between 723 K and 773 K, where the reaction is completed and no over-burned zone exists at the end of the rotary kiln. The overall comparison of these four cases shows that the conversion is quite sensitive to the wall temperature.

4.3.2.4. Thermal power of the process. Based on the steady-state conditions, the thermal power transferred to the bulk material in the rotary kiln at the optimized wall temperature of 773 K is evaluated. The final temperature of the gaseous products is 773 K (see Fig. 20) and the final temperature of the solid phase is 770 K (calculated from the average temperature of the product at the outlet). The thermal power for the heat transferred from the inner wall to the bulk is given in Table 3 calculated from the integration of overall thermal demand for the different steps including sensible heat and latent heat and reaction enthalpy. For 350

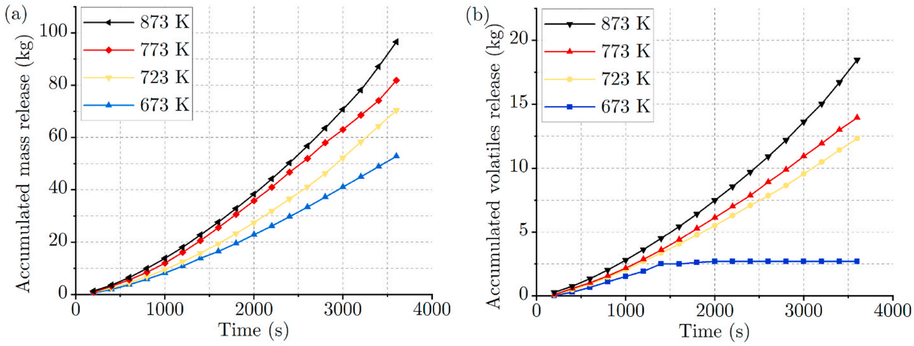

Fig. 16. Accumulative release of moisture (a) and volatiles (b) from the biomass during the conversion.

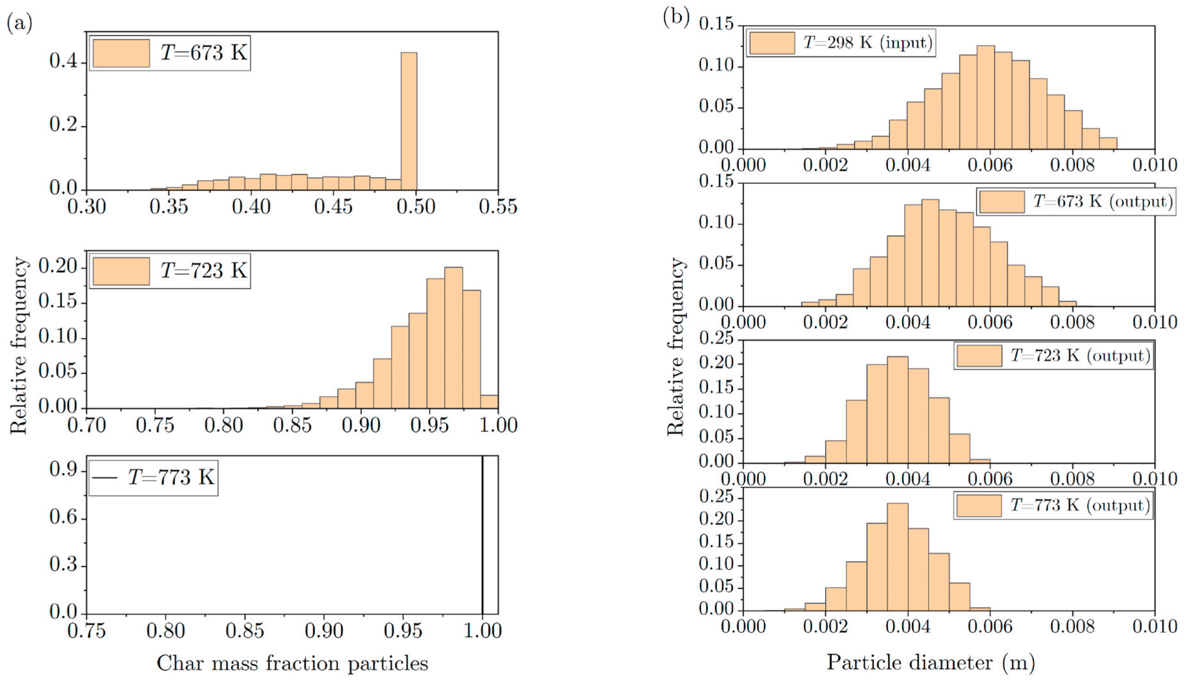

Fig. 17. Char mass fraction of particles (a) and particle size distribution (b) of input and products at different reactor wall temperatures.

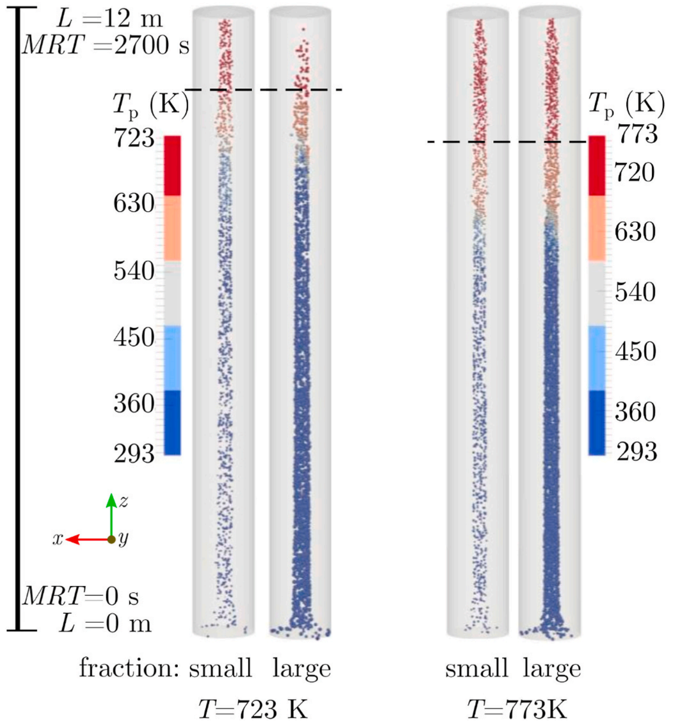

Fig. 18. Effect of particle sizes on their temperatures along the reactor (top view).

kg/h input the inner thermal power of the carbonization reactor is about 180 kW which gives assuming an overall efficiency of $\eta = 0.6$ a total power requirement of about 300 kW_{th}.

The demanded thermal power for drying of the input bulk with 50% MS (yellow zone) in Fig. 19 dominates the sum of the other stages. The portion of the heat flux in each zone approximately corresponds to the length of the stage in the reactor. The thermal power for the reaction contains the power for heating up the dried bulk and gas components as well as the enthalpy of devolatilization. Their shares are 21% and 5.5%, respectively.

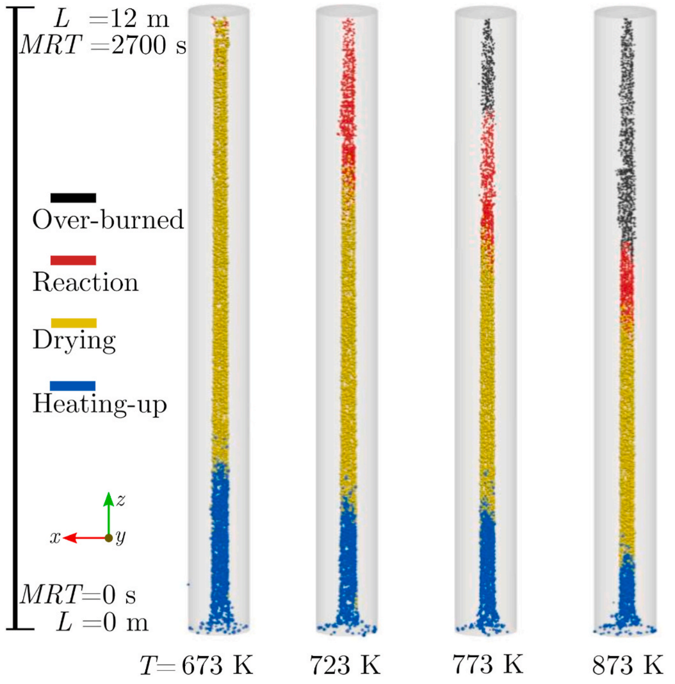

Fig. 19. Stages of the process along the reactor after reaching steady-state (top view).

4.3.2.4. Gas temperature in the rotary kiln. The wet bulk cools down the surrounding gas and as a result, the coldest zone tracks the non-dried bulk in the reactor. The gas-phase temperatures at the bottom of the reactor in Fig. 20 are correlated to the stages of the process given in Fig. 19.

At higher temperatures, the evolution rates of moisture and volatiles become higher, consequently causing higher average velocities in the

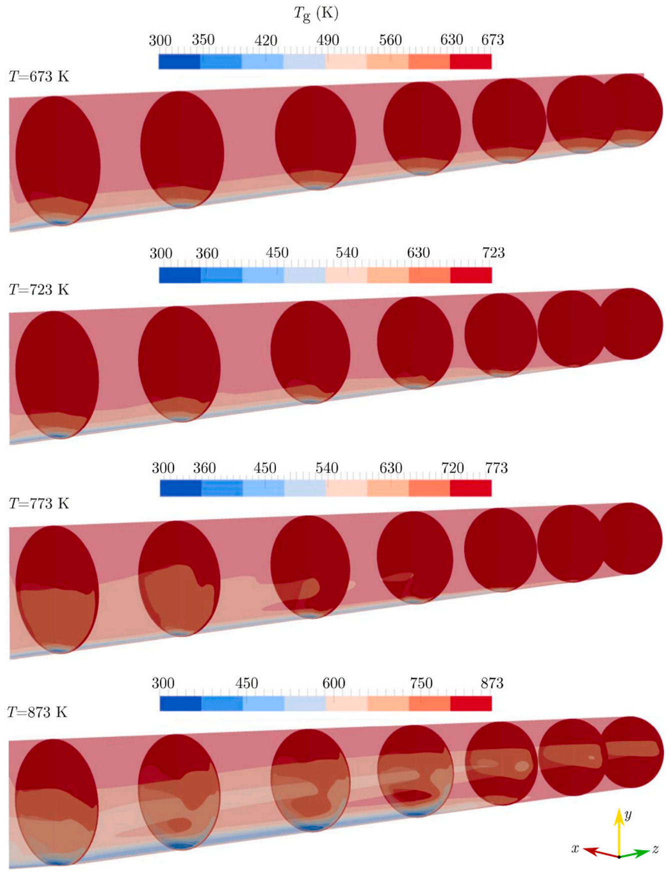

Fig. 20. Gas-phase temperature in the rotary kiln at different wall temperatures (isometric view).

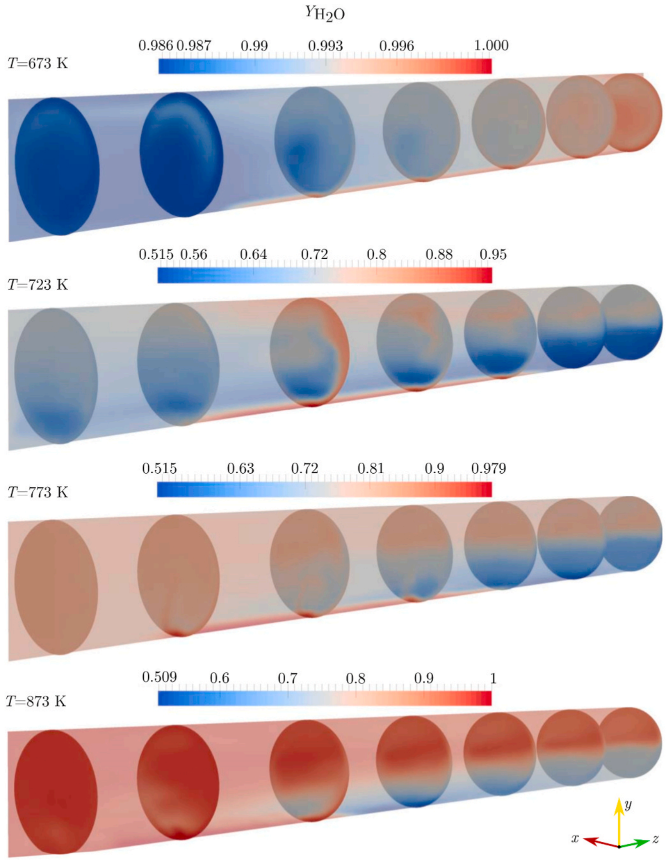

Fig. 21. MS of the gas in the rotary kiln at different wall temperatures (isometric view).

Table 3
Inner thermal power of the rotary kiln reactor.

Process stages	Thermal power (kW)	Thermal power in %
Thermal power to heat up (blue zone)	22.6	12.5
Thermal power to dry the bulk (yellow zone)	109.7	61
Thermal power for the reaction (red zone)	48.3	26.5
Total heat transferred	180.6	100

reactor, see Fig. 16. The accumulative mass release at 873 K is around 15 kg higher than that at 773 K. This amount corresponds to a higher velocity and consequently lower gas residence time in the reactor. It explains why the gas in the hottest reactor, unlike other cases, does not have enough time to reach the final temperature at the end of the reactor. For the 873 K, the outflow velocity of the gas is on average 0.15 m/s with local maxima of 0.45 m/s. The highest velocity in the entire domain is the same in all cases due to the rotation of the kiln and has a value of 0.627 m/s (10 rpm rotation).

4.3.2.5. Moisture and volatiles in the gas-phase. At the steady-state condition, the initial air is completely displaced by the produced steam and volatiles. Fig. 21 depicts the mass fraction of moisture within the reactor, where the rest of the gas are non-condensable volatiles (tar and CO_2). Therefore, the blue color in the figure represents the relatively higher mass fraction of volatiles. The negligible amount of volatiles in the beginning of the reactor at 673 K comes from partial devolatilization of some biomass up to 1500 s before reaching steady-state. The volatiles are gradually being diluted over time (Fig. 16b, blue curve).

For the other cases, the amount of moisture in the first half of the reactor increases with temperature. At the highest temperature, almost only water vapor exists. Drying rate and consequently the velocity are so high that they counteract the penetration of produced volatiles to this area.

The volatiles being produced in the second half of the reactor with increasing wall temperature lead to a shift of the reaction zone more to the inlet. Likewise, the mass fraction of volatiles is reduced due to the dilution with a comparatively larger amount of moisture from the drying zone. The comparison of the amount of moisture and volatiles at the latest points from Fig. 16 confirms the domination of the vapor generation over that of volatiles. As a consequence, gas with a relatively higher mass fraction of moisture is present at the outlet. This shows that some length of the reactor remains effectively unused and the product is over-burned.

5. Conclusion

In this work, a simulation tool is presented to simulate the transient, two-phase and multi-dimensional carbonization of wet biomass in rotary kiln reactors. It is based on the open-source framework OpenFOAM® and combines its Lagrangian capabilities to simulate the biomass particle bed and its Eulerian approach to simulate the gas phase. Both the discrete biomass particles and the multicomponent gas phase are fully coupled. New models for drying, chemical carbonization kinetics and radiation have been developed for the conditions in the rotary kilns and implemented into OpenFOAM®.

A series of validation cases show that the new models are able to accurately simulate the complex physical processes that govern the heating, drying and carbonization inside the reactor. The tool is used to perform a series of simulations for wet biomass carbonization in a rotary kiln reactor at laboratory-scale. Parameter studies regarding biomass mass flow rate, moisture content and wall temperatures reveal the sensitivity of those parameters to biomass conversion and help to choose optimal operating conditions.

The numerical tool is then applied to a large-scale reactor with 350 kg/h biomass throughput. Given real reactor dimensions and biomass mass flow rates an optimal reactor wall temperature can be determined which is 723 K. At this temperature, the conversion rate of the wet biomass to char lies at about 95%. The results also show that the biomass conversion cannot directly be extrapolated from simulation results of the laboratory scale reactor to the large-scale reactor. Therefore, full simulations of the large-scale reactor have to be performed on super-computers. It has been shown, that the new tool can simulate the full process efficiently on up to 560 CPU cores. It is, therefore, suitable for the design of other biomass reactors in the future.

Credit author statement

Salar Tavakkol: development and running of simulations, performing experimental work of wet particulate biomass carbonization, preparing results, writing and editing. Thorsten Zirwes: development and coupling of the main code, implementation of submodel, writing and editing. Jordan Denev: concept development, result prepration, writing and editing. Farshid Jamshidi: preparation and editing of results and editing the text. Nicklas Weber: generation of computational grids, development and implementation of submodels, running parts of simulations tests. Henning Bockhorn: Supervision, improvement and editing the manuscript. Dimosthenis Trimis: project administration, funding acquisition.

Declaration of competing interest

The authors declare that they have no known competing financial interests or personal relationships that could have appeared to influence the work reported in this paper.

Acknowledgments

The authors gratefully acknowledge generous funding of this work by the “Stiftung Energieforschung Baden-Württemberg”, Germany. The authors gratefully acknowledge the Ministry of science, research and arts of the state of Baden-Württemberg, Germany by providing computing time through the Karlsruhe Institute of Technology on the Supercomputer bwUniCluster 1.0 at the Steinbuch Centre for Computing. The fourth author acknowledges the financial support from “Leistungsorientierte Förderung des akademischen Mittelbaus für Forschungsgruppen an HAW”.

References

[1] Demirbas A. Biofuels - securing the planet’s future energy needs. Springer London; 2009.
[2] Basu P. Biomass gasification and pyrolysis. Academic Press (Elsevier); 2010.
[3] Ronsse F, Nachenius RW, Prins W. Carbonization of biomass. In: Recent advances in thermo-chemical conversion of biomass. Elsevier; 2015. p. 293–324.
[4] Appels L, Dewil R. Biomass valorization to energy and value added chemicals: the future of chemical industry. Resour Conserv Recycl 2012;59:1–3. https://doi.org/10.1016/j.resconrec.2011.09.021.
[5] Chen W, Peng J, Bi XT. A state-of-the-art review of biomass torrefaction, densification and applications. Renew Sustain Energy Rev Apr. 2015;44:847–66. https://doi.org/10.1016/j.rser.2014.12.039.
[6] Reichert D, Genova B, Steinbrueck J, Rossbach M, Walz L, Bockhorn H. Biomass steam processing of barley straw towards biocoal – a carbonisation alternative. In: 19th European Biomass Conference & Exhibition; 2011. p. 2027–31.
[7] Steinbrueck J, Reichert D, Genova B, Roßbach M, Walz L, Bockhorn H. Biocoal in minutes – biomass steam processing on the pilot plan scale. In: 20th European Biomass Conference and Exhibition; 2012. p. 2–5.
[8] Steinbrueck J, Walz L, Bockhorn H. Biocoal in minutes - quick and easy source for carbon materials. In: 6th International Conference on Carbon for Energy storage/conversion and environment protection; 2015. p. 45.
[9] Müller-Hagedorn M, Bockhorn H. Pyrolytic behaviour of different biomasses (angiosperms) (maize plants, straws, and wood) in low temperature pyrolysis. J Anal Appl Pyrolysis 2007;79(1–2):136–46. https://doi.org/10.1016/j.jaap.2006.12.008. SPEC. ISS.
[10] Steinbrück J. Biomass Steam Processing Konzeption und Entwicklung eines Verfahrens zur Karbonisierung von Biomasse. Kalrsruhe Institute of Technology; 2019. PhD Thesis.
[11] Steinbrück J, Tavakkol S, Francis G, Bockhorn H. Jatropha – potential of biomass steam processing to convert crop residues to bio-coal and thus triple the marketable energy output per unit plantation area. Ind Crop Prod 2019;136:59–65. https://doi.org/10.1016/j.indcrop.2019.04.065. January.
[12] Sasaki M, Fang Z, Fukushima Y, Adschiri T, Arai K. Dissolution and hydrolysis of cellulose in subcritical and supercritical water. Ind Eng Chem Res 2000;39(8): 2883–90. https://doi.org/10.1021/ie990690j.
[13] Anca-Couce A. Reaction mechanisms and multi-scale modelling of lignocellulosic biomass pyrolysis. Prog Energy Combust Sci 2016;53:41–79. https://doi.org/10.1016/j.pecs.2015.10.002. Mar. 2016.
[14] Van Der Stelt MJC. Chemistry and reaction kinetics of biowaste torrefaction-PhD Thesis. Technische Universiteit Eindhoven; 2010. PhD Thesis.
[15] Xiong Q, Aramideh S, Passalacqua A, Kong SC. BIOTC: an open-source CFD code for simulating biomass fast pyrolysis. Comput Phys Commun 2014;185(6): 1739–46. https://doi.org/10.1016/j.cpc.2014.02.012.
[16] Scherer V, Wirtz S, Krause B, Wissing F. Simulation of reacting moving granular material in furnaces and boilers an overview on the capabilities of the discrete element method. Energy Procedia Aug. 2017;120:41–61. https://doi.org/10.1016/j.egypro.2017.07.154.
[17] Sadhukhan AK, Gupta P, Saha RK. Modelling of pyrolysis of large wood particles. Bioresour Technol Jun. 2009;100(12):3134–9. https://doi.org/10.1016/j.biortech.2009.01.007.
[18] Zhu HP, Zhou ZY, Yang RY, Yu AB. Discrete particle simulation of particulate systems: theoretical developments. Chem Eng Sci 2007;62(13):3378–96. https://doi.org/10.1016/j.ces.2006.12.089.
[19] Zhu HP, Zhou ZY, Yang RY, Yu AB. Discrete particle simulation of particulate systems: a review of major applications and findings. Chem Eng Sci 2008;63(23): 5728–70. https://doi.org/10.1016/j.ces.2008.08.006.
[20] Cundall PA, Strack ODL. A discrete numerical model for granular assemblies. Geotechnique Mar. 1979;29(1):47–65. https://doi.org/10.1680/geot.1979.29.1.47.
[21] Tsuji Y, Tanaka T, Ishida T. Lagrangian numerical simulation of plug flow of cohesionless particles in a horizontal pipe. Powder Technol 1992;71(3):239–50. https://doi.org/10.1016/0032-5910(92)88030-L.
[22] Yamane K, Nakagawa M, Altobelli SA, Tanaka T, Tsuji Y. Steady particulate flows in a horizontal rotating cylinder. Phys Fluids Jun. 1998;10(6):1419–27. https://doi.org/10.1063/1.869858.
[23] Oevermann M, Gerber S, Behrendt F. Euler-Lagrange/DEM simulation of wood gasification in a bubbling fluidized bed reactor. Particuology 2009;7(4):307–16. https://doi.org/10.1016/j.partic.2009.04.004.
[24] Crower CT, Schwarzkopf JD, Sommerfeld M, Tsuji Y. Multiphase with droplets flows wnd particles. CRC Press Taylor & Francis Group; 2012.
[25] Andrews MJ, O’Rourke PJ. The multiphase particle-in-cell (MP-PIC) method for dense particulate flows. Int J Multiphas Flow 1996;22(2):379–402.
[26] Snider DM, O’Rourke PJ, Andrews MJ. An incompressible two-dimensional multiphase particle-in-cell model for dense particle flows. Los Alamos National Laboratory; 1997.
[27] Snider DM, Clark SM, O’Rourke PJ. Eulerian-Lagrangian method for three-dimensional thermal reacting flow with application to coal gasifiers. Chem Eng Sci 2011;66(6):1285–95. https://doi.org/10.1016/j.ces.2010.12.042.
[28] Sazhin SS, Sazhina EM, Faltsi-Saravelou O, Wild P. The p-1 model for thermal radiation transfer: advantages and limitations. Fuel 1996;75(3):289–94. https://doi.org/10.1016/0016-2361(95)00269-3.
[29] Zhong W, Yu A, Zhou G, Xie J, Zhang H. CFD simulation of dense particulate reaction system: approaches, recent advances and applications. Chem Eng Sci 2016;140:16–43. https://doi.org/10.1016/j.ces.2015.09.035.
[30] Klose W, Wiest W. Experiments and mathematical modeling of maize pyrolysis in a rotary kiln. Fuel Jan. 1999;78(1):65–72. https://doi.org/10.1016/S0016-2361(98)00124-0.
[31] Babler MU, Phounglamcheik A, Amovic M, Ljunggren R, Engvall K. Modeling and pilot plant runs of slow biomass pyrolysis in a rotary kiln. Appl Energy Dec. 2017; 207:123–33. https://doi.org/10.1016/j.apenergy.2017.06.034.
[32] Zirwes T, et al. “Quasi-DNS dataset of a piloted flame with inhomogeneous inlet conditions. Flow Turbul Combust Nov. 2019. https://doi.org/10.1007/s10494-019-00081-5.
[33] Nagel WE, Kröner DH, Resch MM. Improved vectorization for efficient chemistry computations in OpenFOAM for large scale combustion simulations. In: High performance computing in science and engineering ’18. Springer; 2018.
[34] Greenshields C, The OpenFOAM Foundation. OpenFOAM user guide. *OpenFOAM Foundation*; 2019. https://cfd.direct/openfoam/user-guide/.
[35] Bryden KM, Ragland KW, Rutland CJ. Modeling thermally thick pyrolysis of wood, 22; 2002. p. 41–53.

[36] Johansen JM, Jensen PA, Glarborg P, Mancini M, Weber R, Mitchell RE. Extension of apparent devolatilization kinetics from thermally thin to thermally thick particles in zero dimensions for woody biomass. Energy 2016;95:279–90. https://doi.org/10.1016/j.energy.2015.11.025.

[37] Parker G, Sutherland AJ. Fluvial armor. J Hydraul Res Sep. 1990;28(5):529–44. https://doi.org/10.1080/00221689009499044.

[38] Chase MW, Curnutt JL, Downey JR, McDonald RA, Syverud AN, Valenzuela EA. JANAF thermochemical tables, 1982 supplement. J Phys Chem Ref Data Jul. 1982; 11(3):695–940. https://doi.org/10.1063/1.555666.

[39] Ku X, Li T, Løvås T. Eulerian–Lagrangian simulation of biomass gasification behavior in a high-temperature entrained-flow reactor. Energy Fuels Aug. 2014;28 (8):5184–96. https://doi.org/10.1021/ef5010557.

[40] Ku X, Li T, Løvås T. CFD-DEM simulation of biomass gasification with steam in a fluidized bed reactor. Chem Eng Sci 2015;122:270–83. https://doi.org/10.1016/j.ces.2014.08.045.

[41] Jang K, Han W, Huh KY. Simulation of a moving-bed reactor and a fluidized-bed reactor by DPM and MPPIC in OpenFOAM®. In: Nóbrega JM, Jasak H, editors. OpenFOAM®. Cham: Springer International Publishing; 2019. p. 419–35.

[42] Tavakkol S, Zirwes T, Denev JA, Weber N, Bockhorn H. Development and validation of an Euler-Lagrange method for the numerical simulation of wet-biomass carbonization in a rotary kiln reactor. 2019.

[43] Mehrabian R, et al. A CFD model for thermal conversion of thermally thick biomass particles. Fuel Process Technol Mar. 2012;95:96–108. https://doi.org/10.1016/j.fuproc.2011.11.021.

[44] Zou B, Gomes AM, R CJ. Studies of superheated fuel spray structures and vaporization in GDI engines. Int J Engine Res 2000;1(4):321–36.

[45] Stanish MA, Schajer GS, Kayihan F. A mathematical model of drying for hygroscopic porous media. AIChE J Aug. 1986;32(8):1301–11. https://doi.org/10.1002/aic.690320808.

[46] Atkins P, de Paula J. Atkins' physical chemistry. tenth ed. Oxford: Oxford University Press; 2014.

[47] Park WC, Atreya A, Baum HR. Experimental and theoretical investigation of heat and mass transfer processes during wood pyrolysis. Combust Flame Mar. 2010;157 (3):481–94. https://doi.org/10.1016/j.combustflame.2009.10.006.

[48] Morf P, Hasler P, Nussbaumer T. Mechanisms and kinetics of homogeneous secondary reactions of tar from continuous pyrolysis of wood chips. Fuel 2002;81 (7):843–53. https://doi.org/10.1016/S0016-2361(01)00216-2.

[49] Müller-Hagedorn M, Bockhorn H, Krebs L, Müller U. Investigation of thermal degradation of three wood species as initial step in combustion of biomass. Proc Combust Inst Jan. 2002;29(1):399–406. https://doi.org/10.1016/S1540-7489(02)80053-0.

[50] Müller-Hagedorn M, Bockhorn H, Krebs L, Müller U. A comparative kinetic study on the pyrolysis of three different wood species. J Anal Appl Pyrolysis 2003;68(69): 231–49. https://doi.org/10.1016/S0165-2370(03)00065-2.

[51] Modest MF. Radiative heat transfer. second ed. San Diego: Academic Press (Elsevier); 1993.

[52] Oliver González A, Vdovin A. Radiation heat transfer in OpenFOAM. Göteborg; 2009 [Online]. Available, http://www.tfd.chalmers.se/~hani/kurser/OS_CFD_2009/AlexeyVdovin/Radiation_in_OpenFoam_final.pdf.

[53] Henein H, Brimacombe JK, Watkinson AP. The modeling of transverse solids motion in rotary kilns. Metall Trans B Jun. 1983;14(2):207–20. https://doi.org/10.1007/BF02661017.

[54] Mellmann J, Specht E. Mathematical modelling of the transition behaviour between the various forms of transverse motion of bulk materials in rotating cylinders part 1 & 2). Cem Lime, Gypsum Int 2001;54:281–96. & 380–402.

[55] Liu XY, Specht E, Mellmann J. Slumping-rolling transition of granular solids in rotary kilns. Chem Eng Sci 2005;60(13):3629–36. https://doi.org/10.1016/j.ces.2005.02.020.

[56] Mellmann J. The transverse motion of solids in rotating cylinders-forms of motion and transition behavior. Powder Technol 2001;118(3):251–70. https://doi.org/10.1016/S0032-5910(00)00402-2.

[57] Asmar BN, Langston PA, Matchett AJ. A generalised mixing index in distinct element method simulation of vibrated particulate beds. Granul Matter Dec. 2002; 4(3):129–38. https://doi.org/10.1007/s10035-002-0112-8.

[58] Sherritt RG, Chaouki J, Mehrotra AK, Behie LA. Axial dispersion in the three-dimensional mixing of particles in a rotating drum reactor. Chem Eng Sci 2003;58 (2):401–15. https://doi.org/10.1016/S0009-2509(02)00551-1.

[59] Solomon PR, Carangelo RM, Best PE, Markham JR, Hamblen DG. The spectral emittance of pulverized coal and char. Symp Combust 1988;21(1):437–46. https://doi.org/10.1016/S0082-0784(88)80271-6.

[60] Graeser P, Schiemann M. "Emissivity of burning bituminous coal char particles – burnout effects. Fuel 2017;196:336–43. https://doi.org/10.1016/j.fuel.2017.01.110.

[61] Wakao N, Kaguei S. Heat and mass transfer in packed beds, vol. 1; 1982.

[62] Shi D, Vargas WL, McCarthy JJ. Heat transfer in rotary kilns with interstitial gases. Chem Eng Sci 2008;63(18):4506–16. https://doi.org/10.1016/j.ces.2008.06.006.

[63] Kim KC, Adrian RJ. Very large-scale motion in the outer layer. Phys Fluids Feb. 1999;11(2):417–22. https://doi.org/10.1063/1.869889.

[64] Washino K, Chan EL, Tanaka T. DEM with attraction forces using reduced particle stiffness. Powder Technol Feb. 2018;325:202–8. https://doi.org/10.1016/j.powtec.2017.11.024.